

Dynamic control of luminescence chirality through achiral metasurfaces

Yawei Wu^{1,2†}, Zhenyu Wang^{1†}, Jiahui Xu³, Chenlu He⁴, Shuqing He⁵, Ruize Wang¹,
Chaowei Wang¹, Dong Wu¹, Jiaru Chu¹, Yiming Wu⁶, Xiaogang Liu^{3*}, Yang Chen^{1*}

¹*Chinese Academy of Sciences Key Laboratory of Mechanical Behavior and Design of Materials,
Department of Precision Machinery and Precision Instrumentation, University of Science and
Technology of China, 230027 Hefei, China*

²*Hefei National Laboratory for Physical Sciences at the Microscale, University of Science and
Technology of China, Hefei Anhui 230026, China*

³*Department of Chemistry, National University of Singapore, 117583 Singapore, Singapore*

⁴*School of Chemistry and Chemical Engineering, Nanjing University of Science and Technology,
Nanjing 210094, China.*

⁵*College of Health Science and Environmental Engineering, Shenzhen Technology University,
518118 Shenzhen, China*

⁶*Institute of Flexible Electronics (IFE, Future Technologies), Xiang'an Campus, Xiamen
University, Xiang'an South Road, Xiamen 361102, Fujian, China*

[†]*These authors contributed equally: Yawei Wu, Zhenyu Wang*

^{*}*Email: chmlx@nus.edu.sg, cyang_phys@ustc.edu.cn*

Abstract

Circularly polarized light (CPL) sources are essential for chiroptics, spintronics, quantum optics, and asymmetric photochemistry. However, conventional approaches fail to simultaneously realize a large luminescence dissymmetry factor (g_{lum}) and wide-range tuning of g_{lum} in a compact device. Chiral luminophores usually suffer from low g_{lum} due to their small molecular sizes. Although chiral metasurfaces can enable a large g_{lum} , they lack post-fabrication tunability. Here, we demonstrate that it is possible to achieve high-purity circularly polarized luminescence using achiral metasurfaces. These metasurfaces enable optical tuning and even reversal of luminescence chirality by uncovering and utilizing giant near-field chirality. We validate our concept with upconversion nanoparticles and downshifting dye molecules, experimentally achieving a large g_{lum} of up to 1.65, which can be actively and continuously tuned between 1.65 and -1.58. Our approach promises important applications in next-generation CPL sources and detectors, and tunable quantum devices.

Main

Circularly polarized light (CPL) carrying spin angular momentum is important for a plethora of applications such as advanced displays¹, chiral sensing², nonlinear optics³, and quantum devices⁴. While luminescence dissymmetry factor (g_{lum}) is the essential figure of merit (FOM) for CPL sources, actively tuning or even reversing g_{lum} in a compact and integrable fashion has become particularly important, considering the ever-growing demand for smart, portable and multifunctional CPL-emitting devices.

Due to the intrinsic chiral nature of CPL, it has been envisioned that CPL emitters must possess chiral structures, either at the molecular scale or at the micro-/nanoscale. Based on this principle,

a variety of chiral luminescent emitters have been developed, but their performance is still quite limited, in terms of the amplitude and tuning range ($|g_{lum}|$ and Δg_{lum}) of g_{lum} , defined as $g_{lum} = 2 \cdot (I_{RCP} - I_{LCP}) / (I_{RCP} + I_{LCP})$. I_{RCP} and I_{LCP} are the right-handed and left-handed circularly polarized (RCP and LCP) components of luminescence. For example, chiral luminescent molecules usually have a very low g_{lum} ⁵⁻¹⁷, in the range from 10^{-5} to 10^{-2} , due to the weak magnetic transition dipole moments, let alone the wide-range tuning of g_{lum} .

Recently, metasurfaces with intrinsic or extrinsic chirality have been harnessed to enable ultracompact, ultrathin CPL-emitting devices with large g_{lum} and strong luminescence intensity¹⁸⁻²⁸. Giant g_{lum} values of over 1.8, which are close to the limit, have been realized based on the mechanisms of bound states in the continuum¹⁹⁻²² and photonic Rashba effects²³. Nevertheless, post-fabrication tunability is still a dilemma. The nanoscale thickness of metasurfaces not only hinders the incorporation of reconfigurable structures that could conduct large deformations, especially in the out-of-plane direction, but also prevents the effective modulation of g_{lum} based on tunable materials, due to the very short light-matter interaction lengths. Helical microstructures can enable a large g_{lum} of luminophores²⁹⁻³¹, and regulate it by external stimuli³²⁻³⁶, but most of them can only switch g_{lum} among several values³³⁻³⁶. Besides, their g_{lum} values are usually irreversible³²⁻³⁵, leading to limited Δg_{lum} .

In general, an ideal CPL-emitting device is anticipated to achieve active and continuous tuning of g_{lum} over the full range from -2 to +2, whose luminescence polarization follows a trajectory from the north pole to the south pole when visualized on the Poincaré sphere (Fig. 1a). However, the conventional notion that CPL emitters must be structurally chiral has hindered the achievement of this goal. Here we report a conceptually new class of nanophotonic CPL-emitting devices in which the luminophores and metasurface, as well as the pump light, are all achiral. Based on Lorentz

reciprocity, the giant near-field chirality hidden in the metasurface is uncovered and assigned to emitted photons. As proof of principle, we demonstrate high-purity circularly polarized luminescence from upconversion nanoparticles (UCNPs) and downshifting dye molecules. A g_{lum} of up to 1.65 is experimentally achieved at room temperature without the use of a static magnetic field, and this value can be actively and continuously tuned over a wide range from 1.65 to -1.58, approaching the performance of an ideal CPL source.

Device design

Our proposed CPL-emitting device consists of a plasmonic metasurface filled with UCNPs (Fig. 1b). Lanthanide-doped UCNPs ($\text{NaYF}_4:30\%\text{Yb},2\%\text{Er}@NaYbF_4$) are first adopted as luminophores, whose core-shell structures together with high concentrations of Yb^{3+} and Er^{3+} result in enhanced upconversion efficiency (see the synthesis process in Supplementary Section 1). Despite their distinct emission peaks, large anti-Stokes shift and good photostability, it is still challenging for UCNPs to generate high-purity circularly polarized luminescence due to the intrinsic crystal lattice symmetry^{37,38}. Our UCNPs exhibit a characteristic photoluminescence (PL) band at around 660 nm when pumped at 980 nm, showing no luminescence chirality (Fig. 1c). The plasmonic metasurface is composed of an array of nanogroove dimers in a gold film, with the two nanogrooves vertically arranged and separated by a nanoscale gap and possessing no structural chirality (see the fabrication process in Methods). SEM images of the metasurface with and without UCNPs are depicted in Fig. 1b. As a result of the strong plasmonic coupling between adjacent nanogroove resonators (see analysis in Supplementary Section 3), two modes are supported by the metasurface: a high-energy antisymmetric mode and a low-energy symmetric mode. Their longitudinal electric field distributions E_z are shown in Fig. 1d. These two modes can be respectively excited by x - and y -polarized light, which is clearly observed in the simulated and

experimental reflection spectra (Fig. 1d).

Near-field chirality and operation principle

When CPL is illuminated at 660 nm, the two modes are simultaneously excited and interfere with each other. Their relative phase delay is controlled by the incident handedness. In the case of RCP light, the interference is constructive in the left groove and destructive in the right groove, leading to the electric field predominantly confined and enhanced in the left groove. The situation is reversed with LCP light (Fig. 2a). Such near-field chirality can be evaluated by defining the quantity of the local circular dichroism (CD): $G(\mathbf{r}) = (|E_{RCP}(\mathbf{r})|^2 - |E_{LCP}(\mathbf{r})|^2) / (|E_{RCP}(\mathbf{r})|^2 + |E_{LCP}(\mathbf{r})|^2)$, where the electric field intensities $|E_{RCP}(\mathbf{r})|^2$ and $|E_{LCP}(\mathbf{r})|^2$ are obtained from the local position \mathbf{r} under RCP and LCP incidence. The local CD is different from the conventionally defined CD measured in the far field. As calculated in Fig. 2a, $G(\mathbf{r})$ maintains ultrahigh values above 0.97 and below -0.97 in the left and right grooves, respectively, but the existence of mirror symmetry forces $G(\mathbf{r})$ to have opposite values on the two sides of the central y - z plane, which cancel each other when transformed to the far field. This is why achiral structures manifest no chiroptical properties when measured in the far field (Fig. S4). For the same reason, the phenomenon of near-field chirality has not been explored until very recently³⁹⁻⁴³.

The strength of near-field chirality is determined by the interference between symmetric and antisymmetric modes. We calculate volume-integrated electric field intensities over the left and right grooves (Σ_{LG} and Σ_{RG}) under RCP incidence (Fig. 2b). Their ratio Σ_{LG}/Σ_{RG} shows a strong resonance with a maximum value of 145 achieved at 660 nm. This wavelength corresponds to the crossing region of the two modes, where they are excited with comparable amplitudes. In metasurface design, this peak wavelength is tailored to overlap with the emission band of UCNPs, so that the maximum near-field chirality can be accessed by emitted photons (see Supplementary

Section 5).

Now that a far-field right-handed circular current source, emitting RCP light at 660 nm, selectively induces an electric field $\mathbf{E}(\mathbf{r})$ in the left groove of the metasurface. According to Lorentz reciprocity, a current source $\mathbf{J}(\mathbf{r})$ positioned in the left groove will in turn generate RCP emission in the far field. The local luminescence dissymmetry factor $g_{lum}(\mathbf{r})$ is directly correlated with the local circular dichroism $G(\mathbf{r})$ by the equation $g_{lum}(\mathbf{r}) = 2G(\mathbf{r})$, which is confirmed in simulations by putting an electric dipole at different locations of the metasurface and analyzing its $g_{lum}(\mathbf{r})$. As depicted in the right column of Fig. 2c, ultrahigh $g_{lum}(\mathbf{r})$ values above 1.95 and below -1.95 are maintained in the left and right grooves, which agrees well with the $G(\mathbf{r})$ distribution in Fig. 2a.

Therefore, if we can selectively deposit luminophores only in the left or right groove during device fabrication, high-purity RCP or LCP luminescence can be generated, but unfortunately this is inaccessible for current nanofabrication techniques. Luminophores are deposited almost equally in the two grooves (Fig. 1b). Alternatively, we can excite luminophores in only one groove by utilizing 980-nm linearly polarized pump light and controlling its orientation angle θ (Fig. 2c, left column). When the linearly polarized light is orthogonal to the left groove ($\theta = 135^\circ$), this groove is individually addressed, whose volume-integrated electric field intensity (Σ_{LG}) is 15 times stronger than the right one (Σ_{RG}) as shown in Fig. 2d. This is because the pump wavelength of 980 nm is spectrally far away from the two coupling modes, leading to very weak near-field interactions between adjacent grooves (see Supplementary section 6). After selective excitation of the left groove, its contained UCNP are locally pumped to the excited states and then undergo near-field non-radiative energy transfer from electrons to the plasmonic mode with giant near-field chirality at 660 nm (Fig. 2c). The PL intensity is boosted by the Purcell effect (Fig. 2c, right

column), and the PL polarization is modulated by the local positive $g_{lum}(\mathbf{r})$ to be RCP. In contrast, when the linearly polarized pump light is orthogonal to the right groove ($\theta = 45^\circ$), LCP luminescence is generated. The overall g_{lum} of the device can be theoretically predicted by the equation:

$$g_{lum}(\lambda_{lum}) = \frac{\iiint_V g_{lum}(\mathbf{r}, \lambda_{lum}) |\mathbf{E}(\mathbf{r}, \lambda_{pump})|^2 d\mathbf{r}}{\iiint_V |\mathbf{E}(\mathbf{r}, \lambda_{pump})|^2 d\mathbf{r}} = \frac{2 \iiint_V CD(\mathbf{r}, \lambda_{lum}) |\mathbf{E}(\mathbf{r}, \lambda_{pump})|^2 d\mathbf{r}}{\iiint_V |\mathbf{E}(\mathbf{r}, \lambda_{pump})|^2 d\mathbf{r}}, \quad (1)$$

where $g_{lum}(\mathbf{r}, \lambda_{lum})$ and $CD(\mathbf{r}, \lambda_{lum})$ are the local luminescence dissymmetry factor and local circular dichroism at the luminescence wavelength, and $|\mathbf{E}(\mathbf{r}, \lambda_{pump})|^2$ is the local electric field intensity at the pump wavelength. The volume integration is conducted over the two grooves where UCNP are present. Accordingly, when pumped at 980 nm, the theoretical g_{lum} spectra are resonant at 660 nm with a peak value of up to 1.8 and -1.8 for the pump polarization $\theta = 135^\circ$ and 45° , corresponding to nearly perfect RCP and LCP emission, respectively.

Dynamic control of upconversion luminescence chirality

To investigate the PL properties of our device, a home-built optical microscope system is utilized (see setup details in Methods). A 980-nm continuous-wave (CW) laser with a power of 30 mW is passed through a linear polarizer, a half-wave plate, and then illuminated on the metasurface. The upconverted luminescence is collected and analyzed with the same objective. When the orientation angle of the pump light θ is set to 135° , the measured RCP component of the PL is much stronger than the LCP one, leading to a g_{lum} value of larger than 1.55 over the emission band from 645 nm to 670 nm. The maximum g_{lum} of 1.65 is acquired at around 660 nm (Fig. 3a), which matches well with our predicted value. The deviation is mainly attributed to fabrication tolerance and unwanted scattering. Moreover, the PL intensity is enhanced 70 times relative to the reference case where UCNP are deposited on a bare gold film (Fig. S8a). The influence of pump power on PL intensity and chirality is provided in Fig. S8b. Once the orientation angle θ is switched to 45° , the obtained

g_{lum} is reversed to -1.58 at around 660 nm (Fig. 3b). If θ is further set to 90° , a negligibly small g_{lum} is obtained over the emission band (Fig. 3c). The PL and g_{lum} spectra measured for other θ values are provided in Supplementary Section 9. In this way, g_{lum} can be continuously tuned within the range from 1.65 to -1.58 by actively controlling θ (Fig. 3d), approximately following the relationship $g_{lum} = -1.64 \cdot \sin(2\theta)$. To the best of our knowledge, this is the largest tuning range Δg_{lum} ever realized for CPL-emitting devices⁴⁴, and the achieved g_{lum} is also record-high for upconverted circularly polarized luminescence.

If the measured PL polarization is mapped on a Poincaré sphere (Fig. 3e), it follows a trajectory from near the north pole to near the south pole, representing a near-perfect CPL source. The polar diagrams of PL polarizations for the cases of $\theta = 45^\circ$ and 135° show typical circular polarization patterns (Fig. 3e, left). We note that the case of $g_{lum} = 0$ for $\theta = 0^\circ$ or 90° does not correspond to linearly polarized emission, but to unpolarized emission composed of an incoherent combination of equivalent RCP and LCP light, because the left and right grooves are equally excited and the contained UCNPs emit incoherently. This is clearly revealed in the polar diagram of polarizations, which differs from the dumbbell-shaped linearly polarized emission (Fig. 3e, right).

Dynamic control of downshifting luminescence chirality

To further demonstrate the universality of our approach, we next achieve dynamic control of downshifting luminescence chirality from 4-(dicyanomethylene)-2-methyl-6-(4-dimethylaminostyryl)-4H-pyran (DCM) dye molecules (Fig. 4a). For reference, a bare DCM-doped PMMA film on glass is measured to have broadband emission centered at 635 nm with $g_{lum} = 0$, when pumped at 520 nm (Fig. 4b). When our designed metasurface is deposited by a 70-nm thick DCM-doped PMMA film, an antisymmetric and a symmetric mode are observed at 577 nm and 641 nm, respectively (Fig. 4b), resulting in maximum near-field chirality achieved within the

emission band of DCM molecules. When a linearly polarized pump laser is used at 520 nm with $\theta = 135^\circ$, a large g_{lum} of 1.24 is obtained (Fig. 4c). By actively controlling the orientation angle θ , g_{lum} can be continuously tuned within the range from 1.24 to -1.08, approximately following the relationship $g_{lum} = -1.16 \cdot \sin(2\theta)$. The PL and g_{lum} spectra for other θ values are included in Supplementary Section 10.

Compared to the UCNPs with narrowband emission, the broadband emission characteristics of DCM molecules provide richer spectral information about the modulation of g_{lum} by near-field chirality. As shown in Fig. 4d, the retrieved g_{lum} exhibits a strong resonance at 610 nm, which corresponds well to the crossing region of the two plasmonic modes in Fig. 4b. Accordingly, we can flexibly tailor the spectral positions of the two modes by different designs of metasurfaces, so that the maximum g_{lum} is customized to a specific wavelength. As demonstrated in Fig. 4d-f, the lineshapes of helicity-resolved PL spectra are significantly modulated by different metasurface designs, and the peak wavelength of g_{lum} is remarkably redshifted from sample 1 to 3 (from left to right). Detailed information of samples 1-3 is provided in Supplementary Section 11. We note that the g_{lum} value realized for DCM molecules is considerably smaller than UCNPs. This is mainly because the near-field chirality $G(\mathbf{r})$ of the metasurface is much weaker outside the grooves than inside them, and rapidly weakens when moving away from the metasurface (see Supplementary Section 12). Compared to UCNPs that are solely deposited inside the grooves, the DCM-doped PMMA film is spin-coated on the metasurface with a considerable thickness. Thus, a higher g_{lum} is anticipated if the thickness of the DCM film can be decreased.

Discussion and Conclusion

In Fig. 5, we compare our approach with some typical chiral luminescent emitters in terms of two key FOMs: $|g_{lum}|$ and Δg_{lum} . Chiral luminophores generally have very poor $|g_{lum}|$ ¹⁴⁻¹⁷. Although

lanthanide complexes⁴⁵ and inorganic crystals⁴⁶ can enable much larger $|g_{lum}|$, their luminescence quantum yields are inevitably decreased as a consequence of the non-radiative decay of excited states⁴⁷, and some of them can only achieve large $|g_{lum}|$ at low temperature⁴⁶. Metasurface-based CPL emitters can achieve giant g_{lum} values, regardless of the chirality of associated luminophores, but they usually lack post-fabrication tunability¹⁸⁻²⁶. Exploiting valley-polarized transition metal dichalcogenides (TMDCs) may offer a possible solution^{27, 28} (Fig. 5), but the atomic thickness of 2D TMDCs restricts the luminescent intensity, and their achieved $|g_{lum}|$ and Δg_{lum} are moderate. Large-scale tuning of g_{lum} is also unattainable based on helical microstructures²⁹⁻³⁶. Moreover, they typically have considerable thicknesses to accumulate $|g_{lum}|$, and possess complicated structures to allow the implementation of external stimuli. In comparison, our device has unprecedented superiority in $|g_{lum}|$ and Δg_{lum} , showing the potential to achieve an ideal CPL-emitting device (Fig. 5). Apart from the two FOMs, our device stands out for its simplicity and ease of operation, as it employs pump light for tuning without needing additional control signals. This approach avoids common issues such as stress fatigue and hysteresis since no structural deformation or material tuning is involved.

In summary, our results represent a paradigm shift in luminescence chirality, demonstrating that it can be optically engineered and reconfigured independently of the structural chirality of emitters. By leveraging the giant chirality hidden in the near-field of the achiral metasurface, we achieve a large g_{lum} of 1.65 and a record-high Δg_{lum} of 3.23 in a compact CPL-emitting device. The generality of our approach allows for its application to various luminescent materials, including gallium arsenide, perovskites, and quantum dots, as well as other frequency conversion processes such as second harmonic generation and spontaneous parametric down-conversion. This paves the way towards next-generation CPL sources and detectors, as well as tunable quantum devices.

References

1. Schadt, M. Liquid crystal materials and liquid crystal displays. *Annual review of materials science* **27**, 305-379 (1997).
2. Ma, W. et al. Attomolar DNA detection with chiral nanorod assemblies. *Nat Commun* **4**, 2689 (2013).
3. Li, G., Zhang, S. & Zentgraf, T. Nonlinear photonic metasurfaces. *Nature Reviews Materials* **2**, 17010 (2017).
4. Lodahl, P. et al. Chiral quantum optics. *Nature* **541**, 473-480 (2017).
5. Zhang, Y. et al. Circularly polarized luminescence in chiral materials. *Matter* **5**, 837-875 (2022).
6. Kumar, J., Nakashima, T. & Kawai, T. Circularly polarized luminescence in chiral molecules and supramolecular assemblies. *The Journal of Physical Chemistry Letters* **6**, 3445-3452 (2015).
7. Longhi, G., Castiglioni, E., Koshoubu, J., Mazzeo, G. & Abbate, S. Circularly polarized luminescence: a review of experimental and theoretical aspects. *Chirality* **28**, 696-707 (2016).
8. Gong, Z.-L. et al. Frontiers in circularly polarized luminescence: molecular design, self-assembly, nanomaterials, and applications. *Science China Chemistry* **64**, 2060-2104 (2021).
9. Sánchez - Carnerero, E.M. et al. Circularly polarized luminescence from simple organic molecules. *Chemistry - A European Journal* **21**, 13488-13500 (2015).
10. Tanaka, H., Inoue, Y. & Mori, T. Circularly polarized luminescence and circular dichroisms in small organic molecules: correlation between excitation and emission dissymmetry factors. *ChemPhotoChem* **2**, 386-402 (2018).
11. Ma, W. et al. Chiral inorganic nanostructures. *Chemical Reviews* **117**, 8041-8093 (2017).
12. Sang, Y., Han, J., Zhao, T., Duan, P. & Liu, M. Circularly Polarized Luminescence in Nanoassemblies: Generation, Amplification, and Application. *Advanced Materials* **32**, e1900110 (2020).
13. Furlan, F. et al. Chiral materials and mechanisms for circularly polarized light-emitting diodes. *Nature Photonics* **18**, 658-668 (2024).
14. Takaishi, K., Hinoide, S., Matsumoto, T. & Ema, T. Axially chiral peri-xanthenoxanthenes as a circularly polarized luminophore. *J Am Chem Soc* **141**, 11852-11857 (2019).
15. Kimoto, T., Tajima, N., Fujiki, M. & Imai, Y. Control of Circularly Polarized Luminescence by Using Open - and Closed - Type Binaphthyl Derivatives with the Same Axial Chirality. *Chemistry - An Asian Journal* **7**, 2836-2841 (2012).
16. Takaishi, K., Iwachido, K. & Ema, T. Solvent-induced sign inversion of circularly polarized luminescence: control of excimer chirality by hydrogen bonding. *J Am Chem Soc* **142**, 1774-1779 (2020).
17. Sawada, Y. et al. Rhodium-catalyzed enantioselective synthesis, crystal structures, and photophysical properties of helically chiral 1, 1' -bitriphenylenes. *J Am Chem Soc* **134**, 4080-4083 (2012).

18. Konishi, K. et al. Circularly polarized light emission from semiconductor planar chiral nanostructures. *Phys Rev Lett* **106**, 057402 (2011).
19. Zhang, X., Liu, Y., Han, J., Kivshar, Y. & Song, Q. Chiral emission from resonant metasurfaces. *Science* **377**, 1215-1218 (2022).
20. Chen, Y. et al. Observation of intrinsic chiral bound states in the continuum. *Nature* **613**, 474-478 (2023).
21. Chen, Y. et al. Compact spin-valley-locked perovskite emission. *Nature Materials* **22**, 1065-1070 (2023).
22. Lim, Y. et al. Maximally chiral emission via chiral quasibound states in the continuum. *Laser & Photonics Reviews* **17**, 2200611 (2023).
23. Rong, K. et al. Spin-valley Rashba monolayer laser. *Nature Materials* **22**, 1085-1093 (2023).
24. Kan, Y. et al. Metasurface - enabled generation of circularly polarized single photons. *Advanced Materials* **32**, 1907832 (2020).
25. Tian, J. et al. Optical rashba effect in a light - emitting perovskite metasurface. *Advanced Materials* **34**, 2109157 (2022).
26. Seo, I.C. et al. Circularly Polarized Emission from Organic-Inorganic Hybrid Perovskites via Chiral Fano Resonances. *ACS nano* **15**, 13781-13793 (2021).
27. Duan, X. et al. Valley-addressable monolayer lasing through spin-controlled Berry phase photonic cavities. *Science* **381**, 1429-1432 (2023).
28. Li, Z. et al. Tailoring MoS2 Valley-Polarized Photoluminescence with Super Chiral Near-Field. *Advanced Materials* **30**, e1801908 (2018).
29. Lu, J. et al. Nano-achiral complex composites for extreme polarization optics. *Nature* **630**, 860-865 (2024).
30. Liu, J. et al. Circularly Polarized Organic Ultralong Room - Temperature Phosphorescence with A High Dissymmetry Factor in Chiral Helical Superstructures. *Advanced Materials* **36**, 2306834 (2024).
31. Zheng, H. et al. Uncovering the circular polarization potential of chiral photonic cellulose films for photonic applications. *Advanced Materials* **30**, 1705948 (2018).
32. Bobrovsky, A. et al. Optically and electrically controlled circularly polarized emission from cholesteric liquid crystal materials doped with semiconductor quantum dots. *Advanced Materials* **24**, 6216 (2012).
33. Yu, H., Zhao, B., Guo, J., Pan, K. & Deng, J. Stimuli-responsive circularly polarized luminescent films with tunable emission. *Journal of Materials Chemistry C* **8**, 1459-1465 (2020).
34. Shi, Y. et al. Recyclable soft photonic crystal film with overall improved circularly polarized luminescence. *Nature Communications* **14**, 6123 (2023).
35. Zhang, X. et al. Mechanically Tunable Circularly Polarized Luminescence of Liquid Crystal - Templated Chiral Perovskite Quantum Dots. *Angew Chem Int Ed Engl* **136**, e202404202 (2024).
36. Qiao, J., Lin, S., Li, J., Tian, J. & Guo, J. Reversible chirality inversion of circularly

- polarized luminescence in a photo-invertible helical cholesteric superstructure. *Chem Commun (Camb)* **55**, 14590-14593 (2019).
37. Kim, J. et al. Monitoring the orientation of rare-earth-doped nanorods for flow shear tomography. *Nature Nanotechnology* **12**, 914-919 (2017).
 38. Zhou, J. et al. Ultrasensitive polarized up-conversion of Tm³⁺-Yb³⁺ doped β -NaYF₄ single nanorod. *Nano Letters* **13**, 2241-2246 (2013).
 39. Chen, Y., Yang, X. & Gao, J. Spin-controlled wavefront shaping with plasmonic chiral geometric metasurfaces. *Light: Science & Applications* **7**, 84 (2018).
 40. Zu, S. et al. Deep-Subwavelength Resolving and Manipulating of Hidden Chirality in Achiral Nanostructures. *ACS nano* **12**, 3908-3916 (2018).
 41. Kim, A.S., Goswami, A., Taghinejad, M. & Cai, W. Phototransformation of achiral metasurfaces into handedness-selectable transient chiral media. *Proc Natl Acad Sci U S A* **121**, e2318713121 (2024).
 42. Horrer, A. et al. Local optical chirality induced by near-field mode interference in achiral plasmonic metamolecules. *Nano Letters* **20**, 509-516 (2019).
 43. Hashiyada, S., Narushima, T. & Okamoto, H. Imaging chirality of optical fields near achiral metal nanostructures excited with linearly polarized light. *ACS Photonics* **5**, 1486-1492 (2018).
 44. Chen, X.M., Zhang, S., Chen, X. & Li, Q. Tunable circularly polarized luminescent supramolecular systems: approaches and applications. *ChemPhotoChem* **6**, e202100256 (2022).
 45. Tan, Y.B. et al. Visible circularly polarized luminescence of octanuclear circular Eu (III) helicate. *J Am Chem Soc* **142**, 17653-17661 (2020).
 46. Ma, J. et al. Chiral 2D perovskites with a high degree of circularly polarized photoluminescence. *ACS nano* **13**, 3659-3665 (2019).
 47. Liu, J. et al. What makes efficient circularly polarised luminescence in the condensed phase: aggregation-induced circular dichroism and light emission. *Chemical Science* **3**, 2737-2747 (2012).

Methods

Numerical simulations.

All simulations in this work are performed using a finite-element-method solver (COMSOL Multiphysics). The permittivity of gold is set based on Johnson and Christy data, while the refractive index of UCNPs and DCM-doped PMMA film is set as 1.45. Periodic boundary conditions are employed in *x*- and *y*-directions, and perfectly matched layers are utilized in the *z*-

direction.

Sample fabrication.

The fabrication process of our device is illustrated in Fig. S2. Firstly, a cleaned silicon wafer is spin-coated with high-resolution electron beam resist HSQ (2wt% in methyl isobutyl ketone, Dow Coming XR-1541) and patterned by electron beam lithography (JEOL-6300FS, acceleration voltage: 100 kV). Secondly, the HSQ pattern is transferred to the underlying silicon substrate by inductively coupled plasma etching (Oxford PlasmaSystem100 ICP380) with a combination of SF₆ and C₄F₈ gases (ICP power: 1300 W, RF power: 50W, temp: 10 °C), with the height of silicon pillars precisely controlled by the etching time. The HSQ mask is then removed by wet etching (BOE). Thirdly, a gold film with a thickness of 160 nm is deposited on the silicon substrate by an electron beam evaporator (AdNaNotek EBS-150). Then, a glass slide is adhered to the surface of the gold film using the optical adhesive OA glue (Norland Products NOA61) and fixed with ultraviolet radiation after curing. Finally, gold nanogrooves on the glass slide are stripped from the silicon substrate.

For the deposition of UCNPs, a solution containing UCNPs at a concentration of 1 mg/ml is sonicated for 1 min to fully disperse the nanoparticles. Then, a 100 µL UCNPs solution is mixed with 1200 µL n-hexane to dilute the concentration. Subsequently, the metasurface sample is placed flat in the solution, with the sample surface slightly lower than the liquid surface, and sonicated for 1 min. Finally, the metasurface sample is taken out and dried naturally. For the deposition of the DCM-doped PMMA film, a 70 nm DCM-doped PMMA film (mass ratio 1:240) is spin-coated onto the metasurface for 40 s at a speed of 6000 rpm.

Optical characterization.

As shown in Fig. S7, for the measurement of upconverted luminescence, a CW laser at 980 nm is

passed through a linear polarizer and a half-wave plate and then focused on the metasurface sample using a 20× objective (NA = 0.4). The upconverted luminescence is collected with the same objective, passed through a low-pass filter to eliminate the influence of pump light, and finally directed to a spectrometer (Horiba, iHR 320). Circular polarization is examined using a combination of a quarter-wave plate and a linear polarizer. To measure downshifting luminescence, the wavelength of the CW laser is changed to 520 nm, while the low-pass filter is replaced by a long-pass filter. All beam splitters utilized are polarization-maintaining.

Acknowledgements

Y.C. acknowledges the support from the National Key Research and Development Project (Grant No. YF2100230012) and National Natural Science Foundation of China (Grant No. 62275241). S.H. acknowledges the support from the National Natural Science Foundation of China (Grant No. 22004087), Natural Science Foundation of Top Talent of SZTU (Grant No. 20200202) and Shenzhen Higher Education Stable Support Program (Grant No. SZWD202206). Yiming W. acknowledges the support from the National Natural Science Foundation of China (Grant Nos. 52372156, 62288102). D.W. acknowledges the support from the National Key Research and Development Project (Grant No. 2021YFF0502700) and National Natural Science Foundation of China (Grant No. 62325507, 61927814). This work was partially carried out at the USTC Center for Micro and Nanoscale Research and Fabrication.

Author contributions

Y.C. conceived the idea. Yawei W. and Y.C. conducted the simulations and designed the experiments. Z.W. conducted the device fabrication. Yawei W. performed the optical characterization. Yawei W., X.L. and Y.C. analyzed the data. Yawei W., X.L. and Y.C. drafted the paper with inputs from all authors. X.L. and Y.C. supervised the project.

Competing interests: The authors declare no competing interest.

Data and materials availability: All data needed to evaluate the conclusions in this paper are available in the main text or the supplementary materials.

Figures and Captions

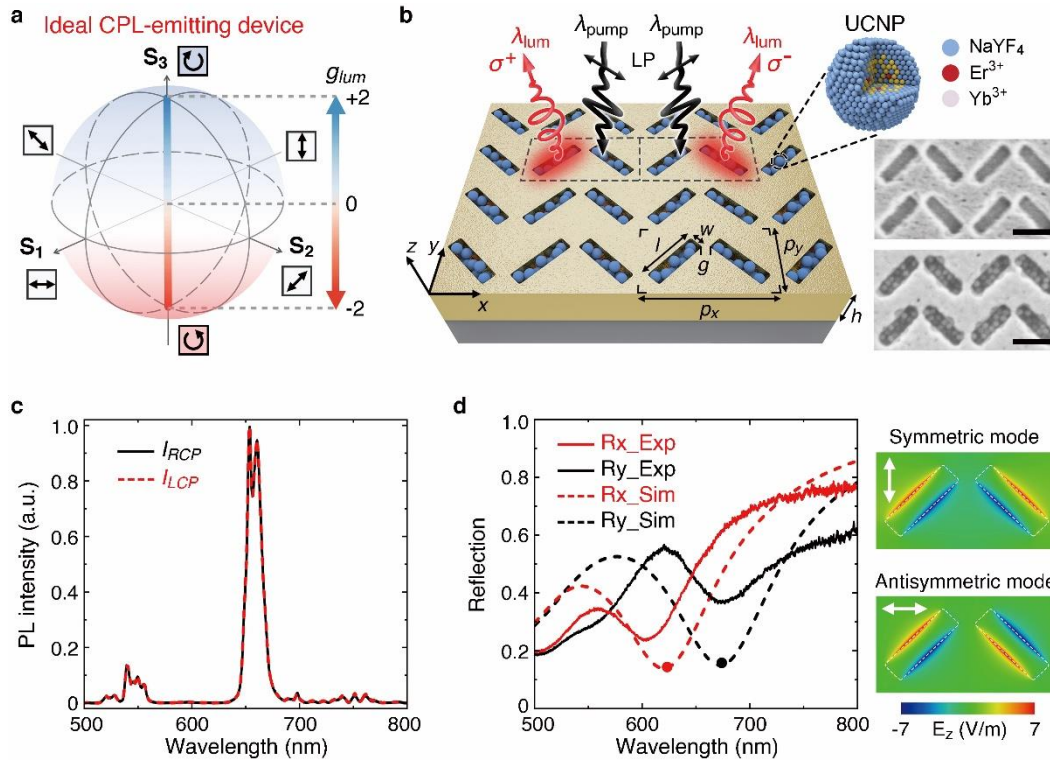


Fig. 1 | Dynamic luminescence chirality control through achiral metasurfaces. **a**, Illustration of an ideal CPL-emitting device in the Poincaré sphere, with its g_{lum} covering the full range from -2 to 2. **b**, Schematic of an achiral plasmonic metasurface enabling chirality-reversible upconverted luminescence from UCNPs. The structural parameters are: $p_x = 382$ nm, $p_y = 210$ nm, $l = 175$ nm, $w = 50$ nm, $g = 40$ nm, gold film thickness $h = 160$ nm, and nanogroove depth $t = 70$ nm. SEM images of the metasurface with (bottom) and without (top) UCNPs are shown on the right. Scale bar, 200 nm. **c**, Helicity-resolved PL spectra from the as-synthesized UCNPs pumped at 980 nm. **d**, Simulated and experimental reflection spectra for the metasurface under x - and y -polarized illuminations. The longitudinal electric field distributions E_z of the symmetric and antisymmetric mode are shown on the right.

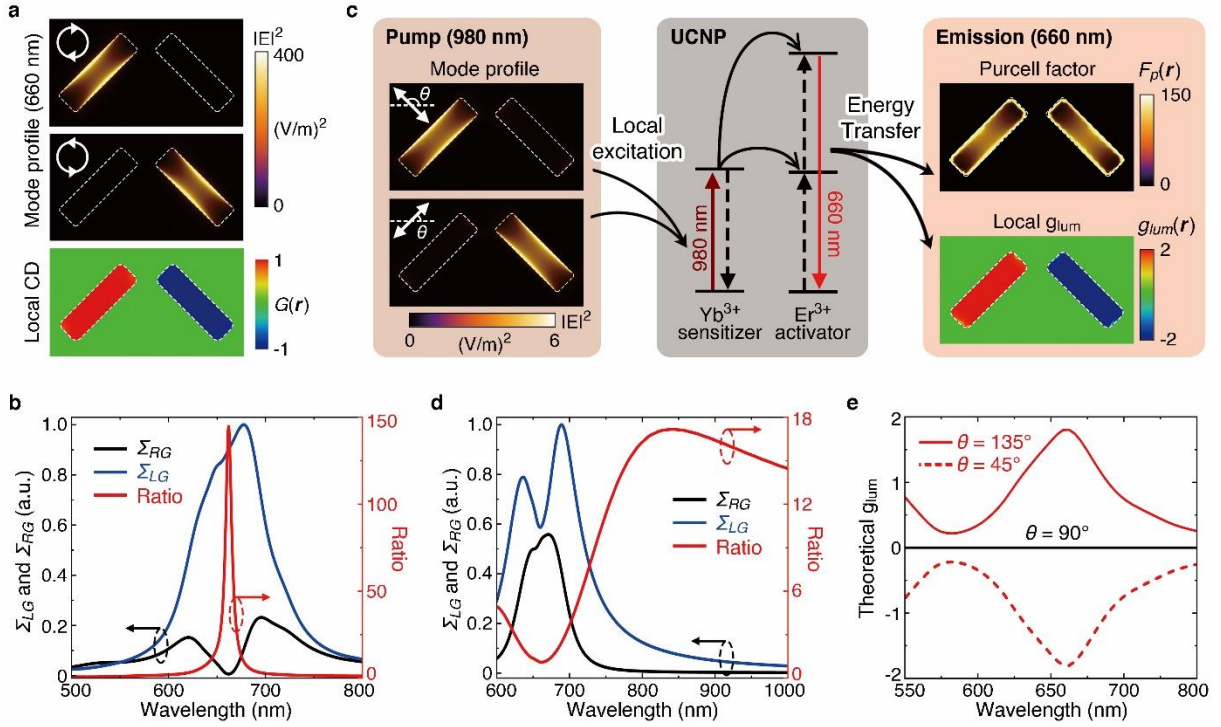


Fig. 2 | Operation principle of the device. **a**, Simulated $|E|^2$ distributions of the metasurface under RCP (top) and LCP (middle) incidence at 660 nm. The corresponding $G(r)$ distributions are shown at the bottom. **b**, **d**, Volume-integrated $|E|^2$ over the left and right groove (Σ_{LG} and Σ_{RG}), along with their ratio (Σ_{LG}/Σ_{RG}), under RCP incidence (**b**) and linearly polarized incidence of $\theta = 135^\circ$ (**d**). **c**, Energy transfer process of our device. When excited by linearly polarized light at 980 nm, the metasurface presents anisotropic $|E|^2$ distributions for $\theta = 45^\circ$ and 135° (left). The contained UCNPs are locally pumped and undergo non-radiative energy transfer from electrons to the plasmonic mode at 660 nm (middle). The luminescence intensity and chirality are thus modulated, with the distributions of Purcell factor $F_p(r)$ and local $g_{lum}(r)$ shown on the right. **e**, Theoretically predicted g_{lum} spectra for the device with pump polarization angles $\theta = 45^\circ$, 90° and 135° .

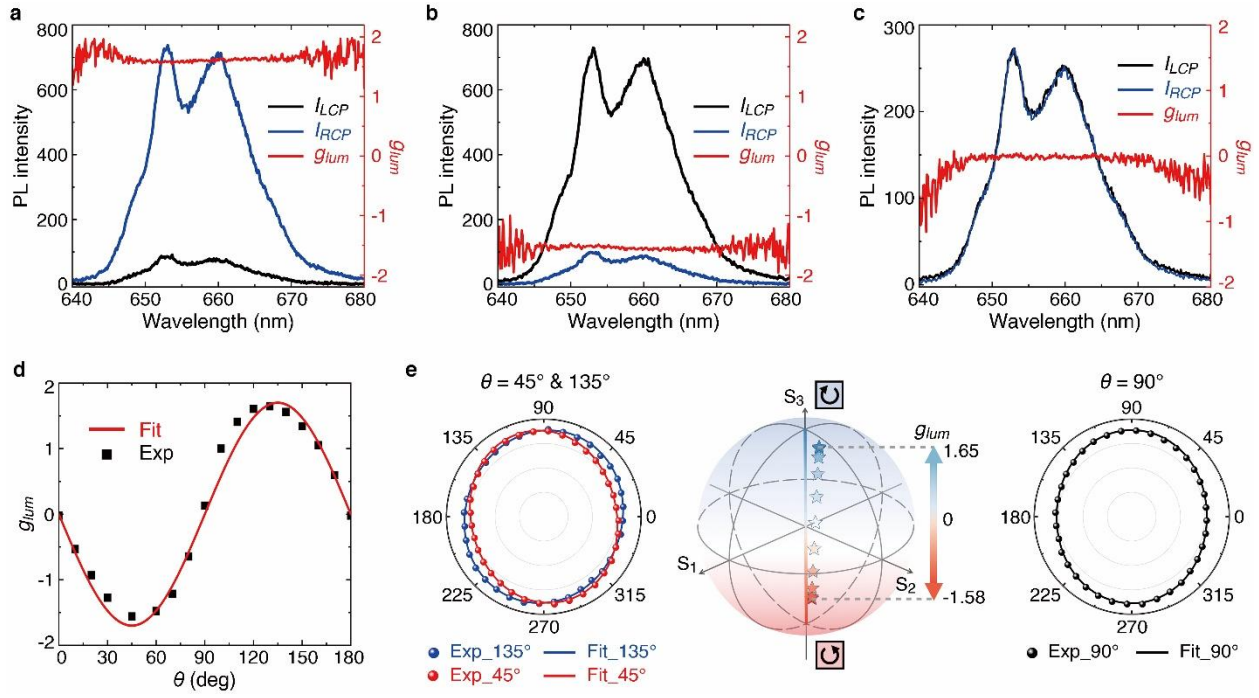


Fig. 3 | Experimental results for chirality-reversible upconverted luminescence. **a-c**, Helicity-resolved PL intensity and g_{lum} spectra measured for pump polarization angles $\theta = 135^\circ$ (**a**), 45° (**b**), and 90° (**c**). **d**, Dependence of experimental g_{lum} values on the polarization angle θ , fitted with a sine function. **e**, Evolution of experimental luminescence polarizations mapped on a Poincaré sphere, represented by colored stars. The polar diagrams of luminescence polarizations for $\theta = 45^\circ/135^\circ$ and $\theta = 90^\circ$ are plotted on the two sides.

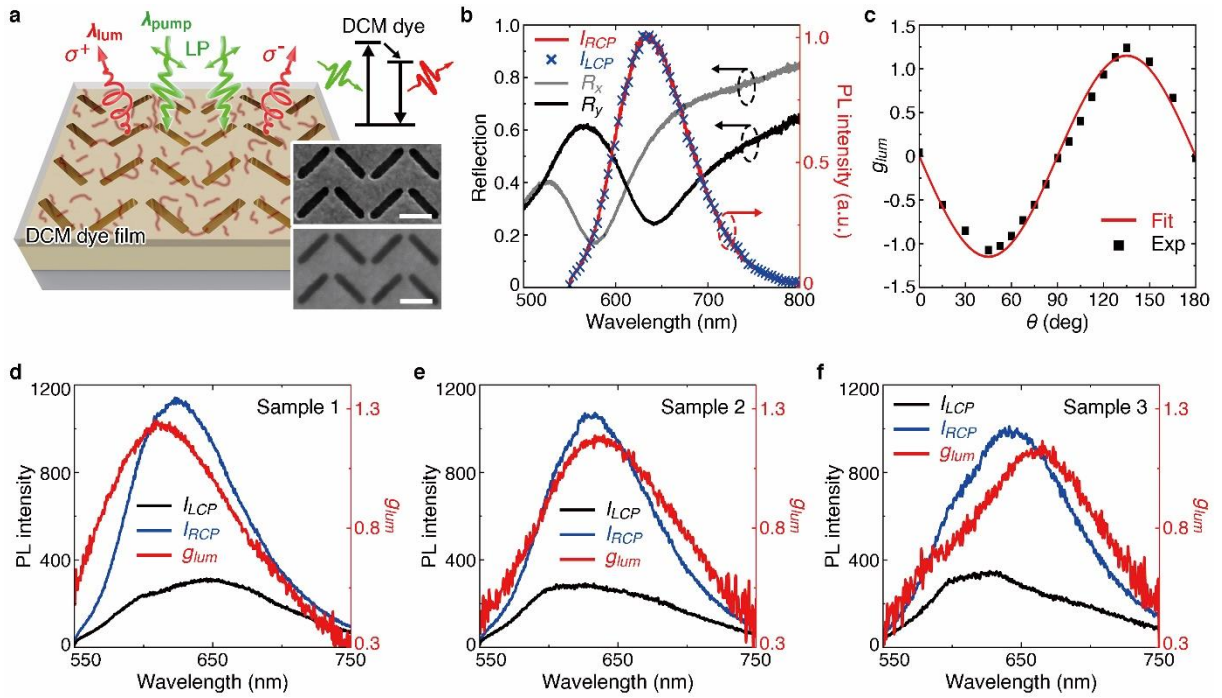


Fig. 4 | Chirality-reversible downshifting luminescence enabled by metasurfaces. a, Schematic of a plasmonic metasurface for achieving chirality-reversible downshifting luminescence from DCM dye molecule film. SEM images of the metasurface before (top) and after (bottom) the spin-coating of the DCM film are depicted on the right. Scale bar: 200 nm. **b,** Experimental reflection spectra of the metasurface under x - and y -polarized illuminations, together with helicity-resolved PL spectra of bare DCM-doped PMMA films pumped at 520 nm. **c,** Dependence of the measured g_{lum} values on the polarization angle θ , fitted with a sine function. **d-f,** Helicity-resolved PL intensity and g_{lum} spectra for different metasurface designs (sample 1-3) at $\theta = 135^\circ$.

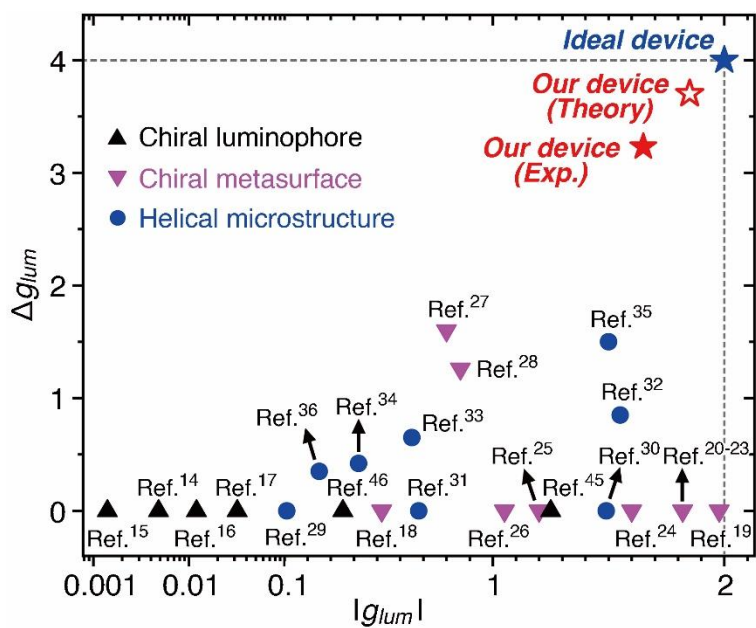


Fig. 5 | Comparison between our approach and some typical chiral luminescent emitters in terms of $|g_{lum}|$ and Δg_{lum} . A logarithmic scale is utilized for the $|g_{lum}|$ axis in the range from 0.001 to 0.1, in order to present the data points of organic chiral molecules.